Observation of Polarization Singularities and Topological Textures in Sound Waves

Ruben D. Muelas-Hurtado,[1,2] Karen Volke-Sepúlveda,[3] Joao L. Ealo,[2,4] Franco Nori,[5,6] Miguel A. Alonso,[7,8] Konstantin Y. Bliokh,[5] and Etienne Brasselet[9]

[1]*School of Civil and Geomatic Engineering, Universidad del Valle, 760032 Cali, Colombia*
[2]*School of Mechanical Engineering, Universidad del Valle, 760032 Cali, Colombia*
[3]*Instituto de Física, Universidad Nacional Autónoma de México, Ciudad de México, 04510, México*
[4]*Centro de Investigación e Innovación en Bioinformática y Fotónica, Universidad del Valle, 760032 Cali, Colombia*
[5]*Theoretical Quantum Physics Laboratory, RIKEN Cluster for Pioneering Research, Wako-shi, Saitama 351-0198, Japan*
[6]*Physics Department, University of Michigan, Ann Arbor, Michigan 48109-1040, USA*
[7]*Aix Marseille Université, CNRS, Centrale Marseille, Institut Fresnel, Marseille, France*
[8]*The Institute of Optics, University of Rochester, Rochester, New York 14627, USA*
[9]*Université Bordeaux, CNRS, LOMA, UMR 5798, F-33400 Talence, France*

(Received 14 July 2022; accepted 10 October 2022; published 8 November 2022)

Polarization singularities and topological polarization structures are generic features of inhomogeneous vector wave fields of any nature. However, their experimental studies mostly remain restricted to optical waves. Here, we report the observation of polarization singularities, topological Möbius-strip structures, and skyrmionic textures in 3D polarization fields of inhomogeneous sound waves. Our experiments are made in the ultrasonic domain using nonparaxial propagating fields generated by space-variant 2D acoustic sources. We also retrieve distributions of the 3D spin density in these fields. Our results open the avenue to investigations and applications of topological features and nontrivial 3D vector properties of structured sound waves.

DOI: 10.1103/PhysRevLett.129.204301

Introduction.—Polarization is an inherent property of monochromatic vector waves, which describes the trajectory of the wave field over its oscillation period. Polarization is routinely used for transverse (e.g., electromagnetic or elastic shear) waves, where it lies in the plane orthogonal to the wave vector $\mathbf{k}$ for a single plane wave and is also responsible for the spin of the wave [1,2]. For longitudinal (e.g., sound) waves, the vector field is collinear with $\mathbf{k}$ for a single plane wave, and it might seem that the polarization properties of such waves are trivial. However, the interference of multiple longitudinal plane waves with different wave vectors $\mathbf{k}_j$, $j = 1, \ldots, N$, causes the polarization at a given point $\mathbf{r}$ to become an ellipse with arbitrary 3D orientation and ellipticity, and hence to have spatially varying spin density [3–6]. Thus, polarization properties of *structured* vector waves share similar generic features independently of the transverse (divergence-free) or longitudinal (curl-free) character of the wave field.

Complex inhomogeneous fields can be characterized via their *singularities* and *topological structures*. Polarization singularities (e.g., the C points or C lines where polarization is circular) have been analyzed in detail for optical fields [7–14], and it was found that the orientation of the 3D polarization ellipse in a vicinity of a generic (nondegenerate) C point has a nontrivial *Möbius-strip* topology [13–20]. Recently, some of us argued that the same topological structures can appear naturally in inhomogeneous sound waves [21] and the present work is in a line of emerging studies of the vector properties of sound waves. First, nonzero spin densities in structured sound waves have recently attracted great attention and offered novel methods of contactless manipulation of objects with sound waves [4,5,22–26]. Second, skyrmionic polarization textures have been recently described and observed in both optical [27–32] and sound [33] waves. Finally, polarization knots were recently analyzed for both optical and sound waves [34–37]. It is worth mentioning that other types of classical waves (e.g., water waves) can also exhibit similar polarization-related features [6,21,36].

Here, we report on the first observation of polarization singularities, polarization Möbius strips, and polarization skyrmionic textures in structured propagating sound waves. We generate nonparaxial Bessel-like sound beams with a pair of C points near the beam center, and also investigate three-wave interference with a periodic lattice of C points. We reconstruct 3D polarization-ellipse distributions of the acoustic velocity field, observe the Möbius-strip topology around the C points, and also retrieve the 3D spin density and identify skyrmionic texture in the propagating field. Our results demonstrate that sound waves exhibit the same rich variety of topological polarization features as optical waves.

Sound waves under consideration.—We consider monochromatic propagating sound waves that can be described

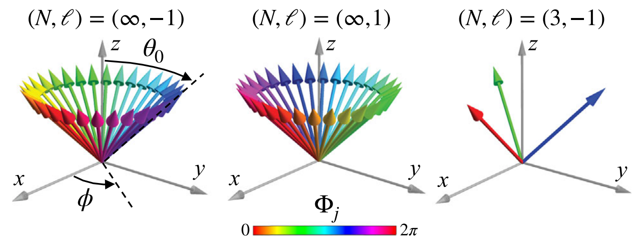

FIG. 1. Wave vectors of N interfering planes waves, Eqs. (1) and (2), evenly distributed over the cone with the polar angle $\theta_0 = \pi/4$ and having relative vortex phases $\Phi_j = \ell\phi$ (color coded). The three cases shown here correspond to the Bessel beams with $\ell = \pm 1$ and a three-wave interference with $\ell = -1$.

by two distinct complex space-variant fields: the scalar pressure field $p(\mathbf{r})$ and the vector velocity field $\mathbf{v}(\mathbf{r}) = -(i/\rho\omega)\nabla p(\mathbf{r})$, where ρ is the mass density of the medium (air, in our case) and ω is the angular frequency. The real time-dependent fields are obtained by applying $\mathrm{Re}[\ldots e^{-i\omega t}]$ to the complex fields p and $\mathbf{v}$ and polarization is described by the velocity field, which can thus be deduced from the gradient of the pressure field.

We consider inhomogeneous sound waves resulting from the superposition of N plane waves with equal amplitudes and wave vectors evenly distributed over the circle $k_z = k \cos\theta_0$, $k = \omega/c$, Fig. 1, where c is the speed of sound. The pressure and velocity fields of this superposition can be written as [21]

$$p = v_0\rho c \sum_{j=1}^{N} \exp(i\mathbf{k}_j \cdot \mathbf{r} + i\Phi_j), \qquad (1)$$

$$\mathbf{v} = v_0 \sum_{j=1}^{N} \bar{\mathbf{k}}_j \exp(i\mathbf{k}_j \cdot \mathbf{r} + i\Phi_j), \qquad (2)$$

where v_0 is the common real-valued velocity amplitude of every constituting plane wave, and $\bar{\mathbf{k}}_j \equiv \mathbf{k}_j/k = (\sin\theta_0\cos\phi_j, \sin\theta_0\sin\phi_j, \cos\theta_0)$ with $\phi_j = 2\pi(j-1)/N$ are the directions of the wave vectors, using spherical angles (θ,ϕ). In addition, we choose the relative phases of the interfering waves to correspond to the vortex with an integer topological charge ℓ, i.e., $\Phi_j = \ell\phi_j$. Specifically, in our experiments we generate fields (1) and (2) with $N = \infty$ (Bessel beams) and $N = 3$ (three-wave interference), topological charges $\ell = \pm 1$, and $\theta_0 = \pi/4$.

The polarization singularities of the vector field $\mathbf{v}$ are the C points [in the 2D (x, y) plane] or C lines (in 3D space) [7–14], which correspond to phase singularities (vortices) of the quadratic scalar field $\mathbf{v}\cdot\mathbf{v}$. We note that, generally, polarization singularities do not coincide with phase singularities of the pressure field. As predicted in Ref. [21], a Bessel beam with $\ell = \pm 1$ has a double-degenerate C point at its center, which can be split into a pair of nondegenerate C points by a perturbation breaking

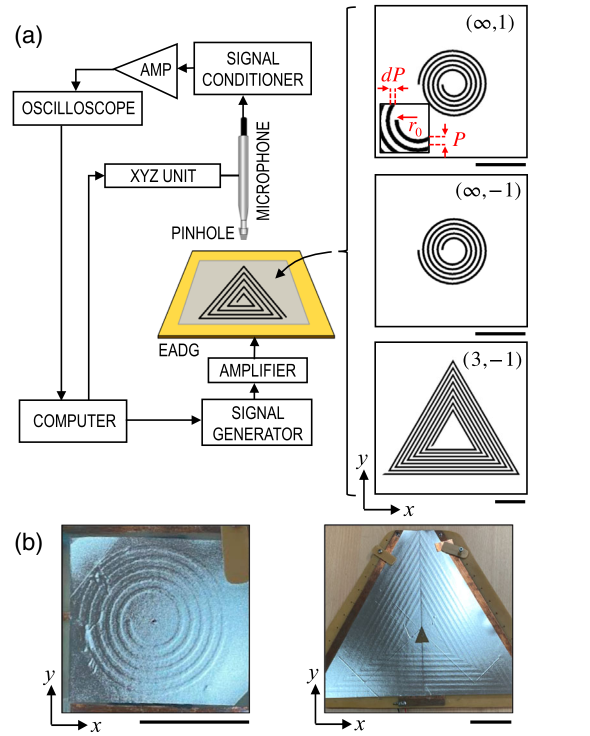

FIG. 2. (a) Sketch of the experimental setup involving 2D structured electroactive diffraction gratings (EADG). (b) Top view of the fabricated acoustic sources corresponding to the Bessel beam with $(N,\ell) = (\infty, 1)$ and three-wave interference $(N,\ell) = (3,-1)$. Scale bars: 5 cm.

the cylindrical symmetry of the field [38–40], whereas the three-wave interference generates a periodic lattice of nondegenerate C points. The orientation of the major axes of the 3D polarization ellipses has a Möbius-strip topology along a closed contour embracing an odd number of nondegenerate C points [13–20].

Experimental setup.—Space-variant ferroelectret-based acoustic transducers, which can be regarded as examples of active acoustic metasurfaces [41], are at the heart of the setup shown in Fig. 2. Their principle of operation is detailed in [42]. This technology allows operating over a broad ultrasonic frequency range 60–300 kHz and offers creating space-variant sources on either flat or developable surfaces. Good acoustic impedance matching with air and user-friendly operation make it a valuable experimental option.

To generate the idealized plane-wave superpositions depicted in Fig. 1 and given by Eqs. (1) and (2), we fabricate three types of flat monolithic electroactive diffracting gratings (EADGs): counterclockwise and clockwise circular spirals for the Bessel beams with $(N,\ell) = (\infty, \pm 1)$ and a clockwise triangular spiral for the three-wave interference $(N,\ell) = (3,-1)$, see Fig. 2. Details on the design, fabrication, and characterization of EADGs for the generation of ultrasonic Bessel beams can be found in [43,44]. Here, the space-variant acoustic transducers are excited with a

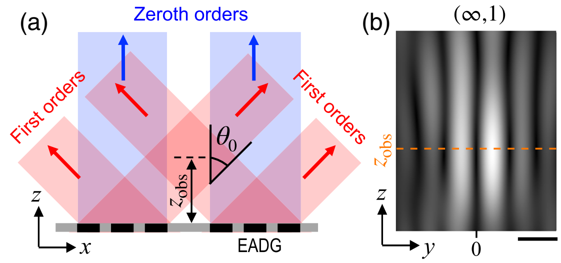

FIG. 3. (a) Side view sketch of the diffraction orders emitted from the structured acoustic source. All space-variant transducers are made to operate at $\theta_0 = \pi/4$ with the observation plane being located at $z_{obs} = 22.5$ mm ($\simeq 6.4\lambda$) for the Bessel beams and $z_{obs} = 50$ mm for the three-wave interference. (b) Numerically simulated amplitude of the pressure field p in the meridional (y, z) plane for the Bessel beam with $\ell = 1$. (For $\ell = -1$ the distribution is mirror symmetric $y \to -y$; the slight asymmetry is due to the broken cylindrical symmetry of the spiral source, Fig. 2.) Scale bars: λ.

computer-controlled 100 V peak-to-peak chirped signal driving a signal generator (Tektronix, Model AFG3022C), connected to a high-speed high-voltage amplifier (Falco System, Model WMA300) for power supply of the EADGs.

The geometrical grating parameters are introduced in Fig. 2 (in red), where $dP = 0.45P$. The desired interference field is generated owing to the first-order diffraction from the grating characterized by the angle $\theta_0 = \pi/4$ [see Fig. 3(a)], which is equivalent to $P = \sqrt{2}\lambda$ where $\lambda = 2\pi c/\omega$ is the wavelength. The azimuth-dependent phase difference between the diffracted waves, $\Phi_j = \ell\phi_j$, is ensured by the geometry of the spiral [43,44]. The circular Bessel-beam spirals have $M = 5$ turns with a minimum radius $r_0 = 10$ mm, and they operate at the frequency $\omega/2\pi = 97$ kHz ($\lambda = 3.5$ mm). The triangular spiral has $M = 8$ turns with $r_0 = 22$ mm (the minimum radial distance to the spiral), and it operates at $\omega/2\pi = 70$ kHz ($\lambda = 4.9$ mm).

In the limit of geometric acoustics the first diffraction orders overlap at axial distances between

$$z_{\min} = r_0 \frac{P}{\lambda}\sqrt{1 - \frac{\lambda^2}{P^2}} \quad \text{and} \quad z_{\max} = z_{\min}\left(1 + \frac{MP}{r_0}\right) \qquad (3)$$

from the acoustic source. Therefore, we obtain the desired fields at a distance $z_{obs} = (z_{\max} + z_{\min})/2$ from the source plane, as shown in Fig. 3(a). Note that $r_0 \neq 0$ prevents the zeroth-order diffracted field to interfere with the desired first-order one in the (x, y) area $r < r_0$ (there are no propagating higher diffraction orders at the frequencies of interest).

Measurements and simulations.—The polychromatic radiated acoustic pressure field (50–200 kHz chirped pulse of 830 μs duration at a repetition rate of 10 Hz) is measured

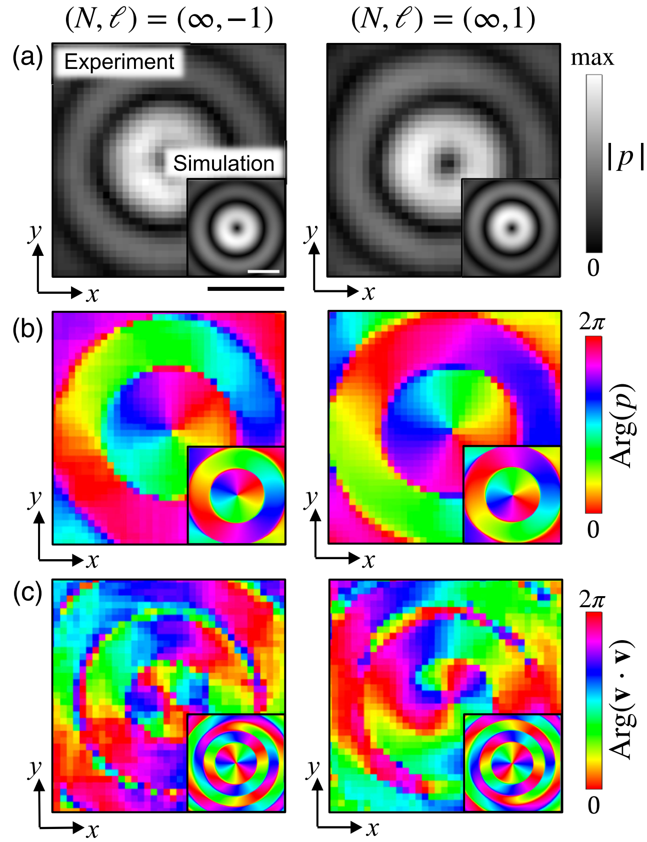

FIG. 4. Experimental (main panels) and numerically simulated (inset panels) transverse (x, y) distributions (at $z = z_{obs}$) of the amplitude (a) and phase (b) of the pressure field p, and of the phase (c) of the quadratic field $\mathbf{v} \cdot \mathbf{v}$ for the Bessel beams with $(N, \ell) = (\infty, \pm 1)$. The charge-$\pm 2$ vortices in $\mathrm{Arg}(\mathbf{v} \cdot \mathbf{v})$ indicate double-degenerate C points of circular polarizations in the beam centers [5,21]. Scale bars: λ.

using a calibrated microphone (1/8 inch, Bruel and Kjaer) whose position is controlled in 3D with an XYZ stage unit. A 0.5 mm diameter pinhole is fitted to the tip of the microphone to increase the spatial resolution of the measurements while preventing diffraction drawbacks [45]. The signal is recorded after being amplified while a real-time monitoring is made with an oscilloscope. Then, we perform a Fourier analysis of the time-domain data, which gives access to both the magnitude and phase of each spectral component of the pressure field with practically negligible noise. The frequency of interest (70 or 97 kHz) is selected according to our design for further data processing.

To reconstruct the 3D inhomogeneous acoustic field, we gather data both in the (x, y) transverse plane, at $z = z_{obs}$, and in the (x, z) meridional plane. Measurements in the transverse plane are made over a squared grid of 12×12 mm^2 [15×15 mm^2] in steps of 0.3 mm corresponding to the (x, y) planes at the distances of $z = (22.8, 23.0, 23.2)$ mm [$z = (50.3, 50.6, 50.9)$ mm] for the Bessel beams $(N, \ell) = (\infty, \pm 1)$ [three-wave interference

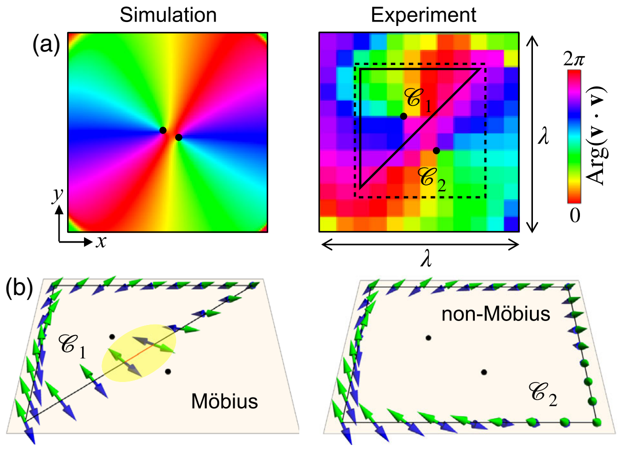

FIG. 5. (a) Fine subwavelength splitting of the double-degenerate C point in the center of the Bessel beam with $\ell = 1$, Fig. 4(c), into a pair of nondegenerate C points due to the slight asymmetry of the spiral source. (b) Experimentally retrieved distributions of the major semiaxes (represented by colored bivectors) of the polarization ellipses of the 3D velocity field $\mathbf{v}$ along the contours $\mathcal{C}_1$ and $\mathcal{C}_2$ embracing one and two C points, respectively. These two configurations correspond to the Möbius-strip (notice the bivector discontinuity highlighted in yellow) and non-Möbius topologies [13].

$(N, \ell) = (3, -1)$]. These values of z are experimentally chosen as optimal and are close to the expected values $z_{\rm obs}$. The distance between the three consecutive z planes and points of the grid in the (x, y) plane allow one to reconstruct the distribution of the vector velocity field $\mathbf{v}(\mathbf{r}) \propto \boldsymbol{\nabla} p(\mathbf{r})$ in the observation (x, y) plane from the calculated gradient of the scalar pressure field. Similar square grids in the (x, z) planes with $y = (-0.2, 0, 0.2)$ mm are used for measurements and reconstruction of the velocity field in the meridional (x, z) plane. For all measurements, the data being shown are evaluated after convolution smoothing of the raw complex pressure field over 5×5 data points.

Numerical validation is performed by simulating the generated acoustic fields based on the Rayleigh diffraction integral for the total radiated pressure field, namely,

$$p(\mathbf{r}) = -i\frac{\rho\omega}{2\pi}\iint_S v_z(\mathbf{r}_s)\frac{\exp(ik|\mathbf{r}-\mathbf{r}_s|)}{|\mathbf{r}-\mathbf{r}_s|}dS, \qquad (4)$$

where $v_z(\mathbf{r}_s)$ is the vertical velocity of the structured transducer at a point $\mathbf{r}_s$ in the $z = 0$ plane. As an example, Fig. 3(b) shows the pressure field magnitude of the Bessel beam with $\ell = 1$ in the meridional plane (y, z).

Results.—Figure 4 shows the results of numerical simulations and experimental measurements of the transverse distributions of the amplitude and phase of the pressure field $p(\mathbf{r})$, as well as of the phase of the quadratic field $\mathbf{v}(\mathbf{r}) \cdot \mathbf{v}(\mathbf{r})$ for the Bessel beams with $\ell = \pm 1$ generated by the circular spirals. One can see the charge-ℓ vortex at the center of the pressure field p and the charge-2ℓ vortex at the center of the $\mathbf{v} \cdot \mathbf{v}$ field. The latter shows the double-degenerate C point at the Bessel-beam center [5,21]. A zoomed-in view on the central area, shown in Fig. 5(a), reveals the fine splitting of the double-degenerate C point into a pair of nondegenerate C points. This splitting occurs because the spiral source is not perfectly cylindrically symmetric, which lifts the central degeneracy in the sound Bessel beam [21,38–40].

Having two nondegenerate C points, we can resolve the polarization Möbius-strip structure around each of these. Figure 5(b) shows the bivectors of the major semiaxes of the polarization ellipses for the 3D velocity field $\mathbf{v}(\mathbf{r})$, retrieved from the experimental data, along the two contours $\mathcal{C}_1$ and $\mathcal{C}_2$ embracing one and two C points. One can see the Möbius and non-Möbius evolutions of the polarization orientations along these contours, in agreement with the theory of polarization singularities [13,15].

Figure 6 shows analogous results of numerical simulations and experimental measurements for the three-wave interference with $\ell = -1$ generated by the triangular spiral. One can see a periodic lattice of charge-± 1 vortices in the pressure field p and in the $\mathbf{v} \cdot \mathbf{v}$ field. Thus, the field exhibits a lattice of nondegenerate C points [21]. Figure 6(b) shows the distribution of the polarization ellipses and their major semiaxis bivectors for the 3D field $\mathbf{v}(\mathbf{r})$ in the vicinity of one of the C points. One can clearly trace the

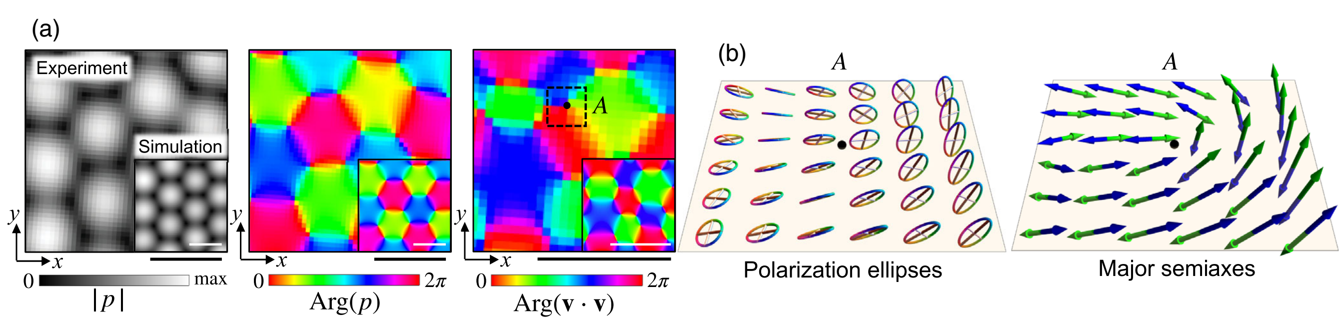

FIG. 6. (a) Same as Fig. 4 but for the three-wave interference field $(N, \ell) = (3, -1)$. The lattice of charge-± 1 vortices in Arg$(\mathbf{v} \cdot \mathbf{v})$ indicate nondegenerate C points [21]. Scale bars: λ. (b) Distributions of the experimentally retrieved 3D polarization ellipses and their major semiaxes for the velocity field $\mathbf{v}$ in the subwavelength area A around one of the C points. One can see the appearance of the Möbius-strip topology around the polarization singularity [15].

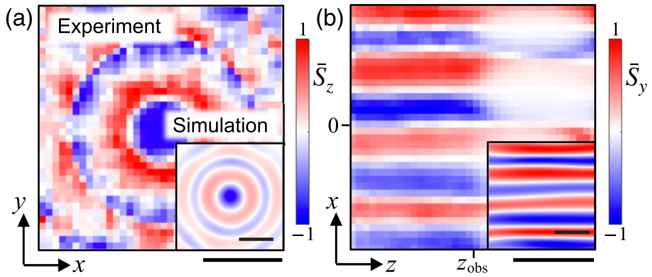

FIG. 7. Experimentally retrieved and numerically calculated (insets) distributions of the longitudinal z and transverse y components of the normalized spin density $\bar{\mathbf{S}}$ in the transverse (x, y) (at $z = z_{obs}$) and meridional (z, x) (at $y = 0$) cross sections of the Bessel beam with $\ell = -1$. Flipping the sign of ℓ flips the sign of $\bar{S}_z$ (see Supplemental Material, Sec. I [46]) but not $\bar{S}_y$ [5]. Scale bars: λ.

appearance of the Möbius-strip topology around the polarization singularity.

It is worth noting that, since we obtain complete information about the vector velocity field $\mathbf{v}(\mathbf{r})$, we can assess experimentally any polarization-related properties of the inhomogeneous sound wave field. This is illustrated in Fig. 7 which displays the longitudinal and transverse components of the normalized 3D spin density $\bar{\mathbf{S}} = \mathrm{Im}(\mathbf{v}^* \times \mathbf{v})/|\mathbf{v}|^2$ in the transverse and meridional cross sections of the Bessel beam with $\ell = -1$, constructed from the measurements. These experimental results, which are supported by numerical simulations, validate recent analytical calculations [5].

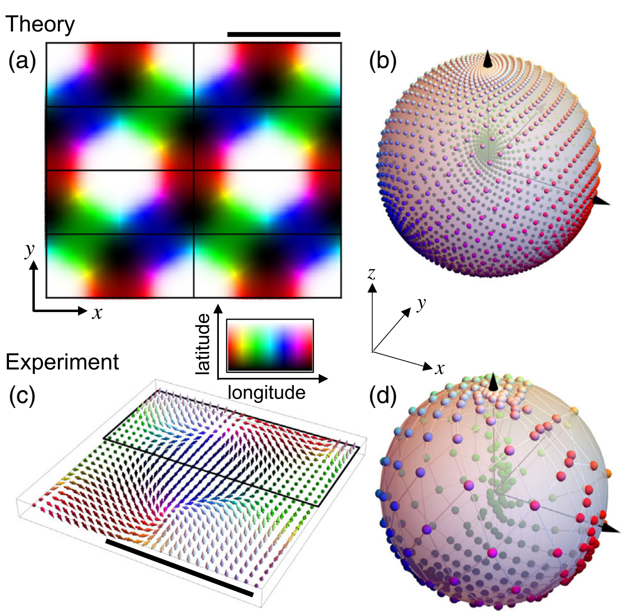

FIG. 8. Theoretical (top row) and experimental (bottom row) coverage of the sphere of velocity field directions for a superposition of three plane waves. In all parts, the direction of the velocity field is encoded as color following the palette at the center. (a) Theoretical distribution of directions for the velocity field over the transverse (x, y) plane, which can be subdivided into cells in which each direction is covered once. (b) Coverage of the sphere of directions for a Cartesian sampling of the (x, y) plane. (c) Velocity field direction distribution for the measured field. (d) Distribution over the sphere of directions for the cell indicated by a rectangle in (c). Scale bars: λ. See also Supplemental Material, Sec. II and Videos 1 and 2 [46].

Also, we find that the distribution of the direction of the instantaneous velocity field $\mathrm{Re}[\mathbf{v}(\mathbf{r})e^{-i\omega t}]$ in the three-wave interference experiment exhibits a lattice of *skyrmions* [27–32], see Fig. 8 and Supplemental Material, Sec. II [46]). This echoes the recent results of Ref. [33] but for propagating acoustic waves rather than for surface standing waves. The temporal behavior of the skyrmionic pattern and the corresponding Skyrme number are discussed in Supplemental Material [46], both for the theoretical and the experimental cases.

Conclusions.—We presented experimental measurements of polarization singularities (C points) and 3D polarization Möbius-strip structures in inhomogeneous sound-wave fields. In doing so, we employed 2D spiral gratings generating nonparaxial interference fields with imprinted vortex properties. By changing the approximate rotational symmetry of the spirals (triangular and circular in our experiments) we controlled the symmetry properties of the generated propagating fields, demonstrating near-degenerate and nondegenerate polarization singularities. In all cases, evolution of the 3D polarization ellipse of the vector velocity field along a contour embracing an odd number of C points exhibits the Möbius-strip topology, in agreement with the general theory of polarization singularities.

We also retrieved nontrivial distributions of the 3D spin density in nonparaxial sound Bessel beams, as well as skyrmionic features in the instantaneous velocity field for a superposition of three plane waves. All generic topological structures we observed are robust against small perturbations, which can be seen from our experimental data exhibiting inevitable distortions. Our results pave the way to further investigations and applications of topological polarization features of 3D vector waves. In addition to the sound waves considered here, one could study other kinds of material waves, such as water waves, elastic waves, etc.

This work was partially funded by project PAPIIT-IN113422 by DGAPA-UNAM, México. R. D. M.-H. acknowledges support from Colciencias Scholarship Program No. 727. J. E. acknowledges support from the Universidad del Valle intramural research Project No. CI21182. F. N. acknowledges partial support from NTT Research, JSPS, and AOARD. M. A. A. and E. B. acknowledge support from the French National Research Agency (ANR) through Award No. ANR-21-CE24-0014-01.

[1] R. M. A. Azzam and N. M. Bashara, *Ellipsometry and Polarized Light* (North-Holland, Amsterdam, 1977).

[2] *The Angular Momentum of Light*, edited by D. L. Andrews and M. Babiker (Cambridge University Press, Cambridge, England, 2012).

[3] W. L. Jones, Asymmetric wave-stress tensors and wave spin, J. Fluid Mech. **58**, 737 (1973).

[4] C. Shi, R. Zhao, Y. Long, S. Yang, Y. Wang, H. Chen, J. Ren, and X. Zhang, Observation of acoustic spin, Natl. Sci. Rev. **6**, 707 (2019).

[5] K. Y. Bliokh and F. Nori, Spin and orbital angular momenta of acoustic beams, Phys. Rev. B **99**, 174310 (2019).

[6] K. Y. Bliokh, H. Punzmann, H. Xia, F. Nori, and M. Shats, Field theory spin and momentum in water waves, Sci. Adv. **8**, eabm1295 (2022).

[7] J. F. Nye and J. V. Hajnal, The wave structure of monochromatic electromagnetic radiation, Proc. R. Soc. A **409**, 21 (1987).

[8] M. V. Berry and M. R. Dennis, Polarization singularities in isotropic random vector waves, Proc. R. Soc. A **457**, 141 (2001).

[9] M. R. Dennis, Polarization singularities in paraxial vector fields: Morphology and statistics, Opt. Commun. **213**, 201 (2002).

[10] F. Flossmann, U. T. Schwarz, M. Maier, and M. R. Dennis, Polarization Singularities from Unfolding an Optical Vortex Through a Birefringent Crystal, Phys. Rev. Lett. **95**, 253901 (2005).

[11] L. D. Angelis, F. Alpeggiani, and L. Kuipers, Spatial Bunching of Same-Index Polarization Singularities in Two-Dimensional Random Vector Waves, Phys. Rev. X **8**, 041012 (2018).

[12] M. R. Dennis, K. O'Holleran, and M. J. Padgett, Singular optics: Optical vortices and polarization singularities, Prog. Opt. **53**, 293 (2009).

[13] K. Y. Bliokh, M. A. Alonso, and M. R. Dennis, Geometric phases in 2D and 3D polarized fields: Geometrical, dynamical, and topological aspects, Rep. Prog. Phys. **82**, 122401 (2019).

[14] Q. Wang, C.-H. Tu, Y.-N. Li, and H.-T. Wang, Polarization singularities: Progress, fundamental physics, and prospects, APL Photonics **6**, 040901 (2021).

[15] I. Freund, Optical Möbius strips in three-dimensional ellipse fields: I. Lines of circular polarization, Opt. Commun. **283**, 1 (2010).

[16] M. R. Dennis, R. P. King, B. Jack, K. O'Holleran, and M. J. Padgett, Isolated optical vortex knots, Nat. Phys. **6**, 118 (2010).

[17] T. Bauer, P. Banzer, E. Karimi, S. Orlov, A. Rubano, L. Marrucci, E. Santamato, R. W. Boyd, and G. Leuchs, Observation of optical polarization Möbius strips, Science **347**, 964 (2015).

[18] E. J. Galvez, I. Dutta, K. Beach, J. J. Zeosky, J. A. Jones, and B. Khajavi, Multitwist Möbius strips and twisted ribbons in the polarization of paraxial light beams, Sci. Rep. **7**, 13653 (2017).

[19] T. Bauer, P. Banzer, F. Bouchard, S. Orlov, L. Marrucci, E. Santamato, R. W. Boyd, E. Karimi, and G. Leuchs, Multitwist polarization ribbon topologies in highly-confined optical fields, New J. Phys. **21**, 053020 (2019).

[20] K. Tekce, E. Otte, and C. Denz, Optical singularities and Möbius strip arrays in tailored non-paraxial light fields, Opt. Express **27**, 29685 (2019).

[21] K. Y. Bliokh, M. A. Alonso, D. Sugic, M. Perrin, F. Nori, and E. Brasselet, Polarization singularities and Möbius strips in sound and water-surface waves, Phys. Fluids **33**, 077122 (2021).

[22] I. D. Toftul, K. Y. Bliokh, M. I. Petrov, and F. Nori, Acoustic Radiation Force and Torque on Small Particles as Measures of the Canonical Momentum and Spin Densities, Phys. Rev. Lett. **123**, 183901 (2019).

[23] Y. Long, D. Zhang, C. Yang, J. Ge, H. Chen, and J. Ren, Realization of acoustic spin transport in metasurface waveguides, Nat. Commun. **11**, 4716 (2020).

[24] Y. Long, H. Ge, D. Zhang, X. Xu, J. Ren, M.-H. Lu, M. Bao, H. Chen, and Y.-F. Chen, Symmetry selective directionality in near-field acoustics, Natl. Sci. Rev. **7**, 1024 (2020).

[25] L. Wei and F. J. Rodriguez-Fortuno, Far-field and near-field directionality in acoustic scattering, New J. Phys. **22**, 083016 (2020).

[26] S. Wang, G. Zhang, X. Wang, Q. Tong, J. Li, and G. Ma, Spin-orbit interactions of transverse sound, Nat. Commun. **12**, 6125 (2021).

[27] A. M. Beckley, T. G. Brown, and M. A. Alonso, Full Poincaré beams, Opt. Express **18**, 10777 (2010).

[28] S. Donati, L. Dominici, G. Dagvadorj, D. Ballarini, M. D. Giorgi, A. Bramati, G. Gigli, Y. G. Rubo, M. H. Szymańska, and D. Sanvitto, Twist of generalized skyrmions and spin vortices in a polariton superfluid, Proc. Natl. Acad. Sci. U.S.A. **113**, 14926 (2016).

[29] S. Tsesses, E. Ostrovsky, K. Cohen, B. Gjonaj, N. H. Lindner, and G. Bartal, Optical skyrmion lattice in evanescent electromagnetic fields, Science **361**, 993 (2018).

[30] L. Du, A. Yang, A. V. Zayats, and X. Yuan, Deep-subwavelength features of photonic skyrmions in a confined electromagnetic field with orbital angular momentum, Nat. Phys. **15**, 650 (2019).

[31] S. Gao, F. C. Speirits, F. Castellucci, S. Franke-Arnold, S. M. Barnett, and J. B. Götte, Paraxial skyrmionic beams, Phys. Rev. A **102**, 053513 (2020).

[32] D. Sugic, R. Droop, E. Otte, D. Ehrmanntraut, F. Nori, J. Ruostekoski, C. Denz, and M. R. Dennis, Particle-like topologies in light, Nat. Commun. **12**, 6785 (2021).

[33] H. Ge, X.-Y. Xu, L. Liu, R. Xu, Z.-K. Lin, S.-Y. Yu, M. Bao, J.-H. Jiang, M.-H. Lu, and Y.-F. Chen, Observation of Acoustic Skyrmions, Phys. Rev. Lett. **127**, 144502 (2021).

[34] H. Larocque, D. Sugic, D. Mortimer, A. J. Taylor, R. Fickler, R. W. Boyd, M. R. Dennis, and E. Karimi, Reconstructing the topology of optical polarization knots, Nat. Phys. **14**, 1079 (2018).

[35] E. Pisanty, G. J. Machado, V. Vicuña-Hernández, A. Picón, A. Celi, J. P. Torres, and M. Lewenstein, Knotting fractional-order knots with the polarization state of light, Nat. Photonics **13**, 569 (2019).

[36] D. Sugic, M. R. Dennis, F. Nori, and K. Y. Bliokh, Knotted polarizations and spin in 3D polychromatic waves, Phys. Rev. Res. **2**, 042045(R) (2020).

[37] M. F. Ferrer-Garcia, A. D'Errico, H. Larocque, A. Sit, and E. Karimi, Polychromatic electric field knots, Phys. Rev. Res. **3**, 033226 (2021).

[38] K. Y. Bliokh, A. Niv, V. Kleiner, and E. Hasman, Singular polarimetry: Evolution of polarization singularities in electromagnetic waves propagating in a weakly anisotropic medium, Opt. Express **16**, 695 (2008).

[39] S. Vyas, Y. Kozawa, and S. Sato, Polarization singularities in superposition of vector beams, Opt. Express **21**, 8972 (2013).

[40] E. Otte, C. Alpmann, and C. Denz, Polarization singularity explosions in tailored light fields, Laser Photonics Rev. **12**, 1700200 (2018).

[41] B. Assouar, B. Liang, Y. Wu, Y. Li, J.-C. Cheng, and Y. Jing, Acoustic metasurfaces, Nat. Rev. Mater. **3**, 460 (2018).

[42] J. L. Ealo, J. J. Camacho, and C. Fritsch, Airborne ultrasonic phased arrays using ferroelectrets: A new fabrication approach, IEEE Trans. Ultrason. Ferroelectr. Freq. Control **56**, 848 (2009).

[43] R. D. Muelas-Hurtado, J. L. Ealo, J. F. Pazos-Ospina, and K. Volke-Sepulveda, Generation of multiple vortex beam by means of active diffraction gratings, Appl. Phys. Lett. **112**, 084101 (2018).

[44] R. D. Muelas-Hurtado, J. L. Ealo, J. F. Pazos-Ospina, and K. Volke-Sepulveda, Acoustic analysis of a broadband spiral source for the simultaneous generation of multiple Bessel vortices in air, J. Acoust. Soc. Am. **144**, 3252 (2018).

[45] K. Sasaki, M. Nishihira, and K. Imano, Low-frequency air-coupled ultrasonic system beyond diffraction limit using pinhole, Jpn. J. Appl. Phys. **45**, 4560 (2006).

[46] See Supplemental Material at http://link.aps.org/supplemental/10.1103/PhysRevLett.129.204301 for additional experimental and numerical data both for the spin density and the Skyrme number.